Journal of The
Electrochemical Society

Distribution of Relaxation Times Analysis for Impedance Spectra Containing Resistive-Inductive Characteristics: Part I. Deconvolution Methods

To cite this article: Christian Plank *et al* 2025 *J. Electrochem. Soc.* **172** 060514

Journal of The Electrochemical Society, 2025 **172** 060514

Distribution of Relaxation Times Analysis for Impedance Spectra Containing Resistive-Inductive Characteristics: Part I. Deconvolution Methods

Christian Plank,[1,2,=,z] Tobias G. Bergmann,[3,=] Nicolas Schlüter,[3] and Michael A. Danzer[1,2]

[1]*Chair of Electrical Energy Systems, University of Bayreuth, Universitätsstraße 30, Bayreuth, 95447, Bavaria, Germany*
[2]*Bavarian Center for Battery Technology, University of Bayreuth, Universitätsstraße 30, Bayreuth, 95447, Bavaria, Germany*
[3]*Institute of Environmental and Sustainable Chemistry, Technical University of Braunschweig, Hagenring 30, Brunswick, 38106, Lower Saxony, Germany*

The distribution of relaxation times analysis is a powerful and non-destructive technique based on electrochemical impedance spectroscopy to analyze and identify electrochemical reactions and processes in batteries, fuel cells, and other electrochemical systems. However, there are inherent challenges to this analysis method that affect the accuracy of the results and impede their interpretation, particularly when capacitive, inductive or resistive-inductive characteristics are present. In this case, data truncation is often used, which leads to incorrectly identified time constants and polarization contributions as well as an ohmic offset. An approach that is capable of analyzing arbitrary spectra and determining the true ohmic offset is presented and applied to three algorithms to evaluate the influence of different regularization techniques: the generalized DRT analysis, the VanCittert algorithm and the separated sparse spike deconvolution. To validate the results, they are compared to the electrochemical system analysis (ELSA), which is a complementary data-driven method. It can be demonstrated that the proposed approach efficiently handles resistive-capacitive and resistive-inductive effects without requiring any non-negativity constraint for the parameters nor data truncation and without adding complexity.
 [DOI: 10.1149/1945-7111/adda7b]

Manuscript submitted April 1, 2025; revised manuscript received May 9, 2025. Published June 10, 2025.

In 1941 an important milestone in the Electrochemical Impedance Spectroscopy (EIS) has been achieved by Cole and Cole[1] with the representation of impedance in the complex plane, which is known as Cole-Cole-plot. Since then, EIS[2] has found increasing interest in several fields.[3–6] It is a powerful, non-invasive and non-destructive measuring technique that is widely used to study various electrochemical reactions and processes on material, component, and system level, e.g. for batteries, fuel cells, sensors and corrosion processes.[7–11] Examples are electrical and ionic conductivities,[12,13] characterization of processes like charge transfer [14] and solid state diffusion,[15] study of aging mechanisms[16] or estimation of state of charge and state of health.[10,17] The processes found in electrochemical systems (e.g. charge transfer, ionic conductivity, solid state diffusion) can be simulated using equivalent circuit models (ECM). However, employing ECMs requires *a priori* knowledge of the underlying system and its expected number and type of processes, which hinders its use for novel materials or systems. The distribution of relaxation times analysis (DRT) aims to reduce the necessary prior knowledge by not requiring a particular model. Instead of the model parameters, the analysis provides a distribution function, which represents the polarization of resistive-capacitive elements over a range of time constants. The course of the distribution function typically shows distinct peaks that can be utilized to identify and characterize processes.[18–20] For this reason, the method has recently been increasingly used for a wide variety of applications, such as the characterization of new materials,[21–23] degradation studies[16,24] or cell-to-cell variation studies.[25–27]

However, despite its growing popularity and all the improvements that have been made, the method still faces limitations and challenges. One of its main limitations is a strong dependence on the choice of deconvolution method, which affects the shape and smoothness of the peaks, thus limiting the minimum peak proximity required for successful separation. It also imposes restrictions on which features in the impedance spectrum can be analyzed. As shown in Fig. 1, this results in the following critical challenges that need to be addressed: (I) impedance spectra exhibiting resistive-inductive behavior, (II) divergent features such as inductive or capacitive characteristics, and (III) the ohmic offset of the system. This paper is the first in a series of publications focusing on these challenges. The second paper examines how different regularization strategies and constraints affect the distribution function and the determination of the ohmic offset, the third paper focuses on the application of the improved methods to allow a reliable interpretation of the results, and the present work starts with the mathematical background of different deconvolution methods and the necessary modifications for an efficient analysis of spectra containing resistive-inductive contributions.

Electrochemical systems such as batteries and fuel cells often exhibit not only resistive-capacitive behavior, but also resistive-inductive effects, as shown in Fig. 2. In the context of batteries, this phenomenon can mainly be attributed to either the wiring, the cell winding[28] or the electromagnetic skin effect.[29] All manifest as resistive-inductive contributions in the high-frequency range. In contrast, PEM fuel cells exhibit low-frequency resistive-inductive effects. The origin of the observation has not yet been conclusively clarified and is still discussed in the literature. The most plausible explanations attribute it to a multistep reaction with intermediate species of the oxygen reduction reduction (ORR) site, water transport characteristics, and carbon monoxide poisoning.[30–34] However, both of these resistive-inductive behaviors cause a visual shift in the real part of the impedance, demonstrating that the visible zero-crossing resistance does not reflect the true resistance of the system. This highlights the importance of adapting the deconvolution methods to analyze these effects, determine the true ohmic offset, and to avoid having to preprocess the data by truncation. In order to extend the DRT approach, Danzer[28] added a second distribution function for resistive-inductive features. Later, Huang et al.[35] proposed that this can be omitted if negative polarization is allowed in the distribution function. This is an interesting approach, as it significantly reduces computational effort. However, this change has two aspects that must be considered. First, according to Huang et al., the obtained ohmic offset must be corrected, and second, negative polarization has no meaningful physical interpretation in the context of a distribution function. The question of whether

[=]Equal Contribution.
[z]E-mail: christian.plank@uni-bayreuth.de

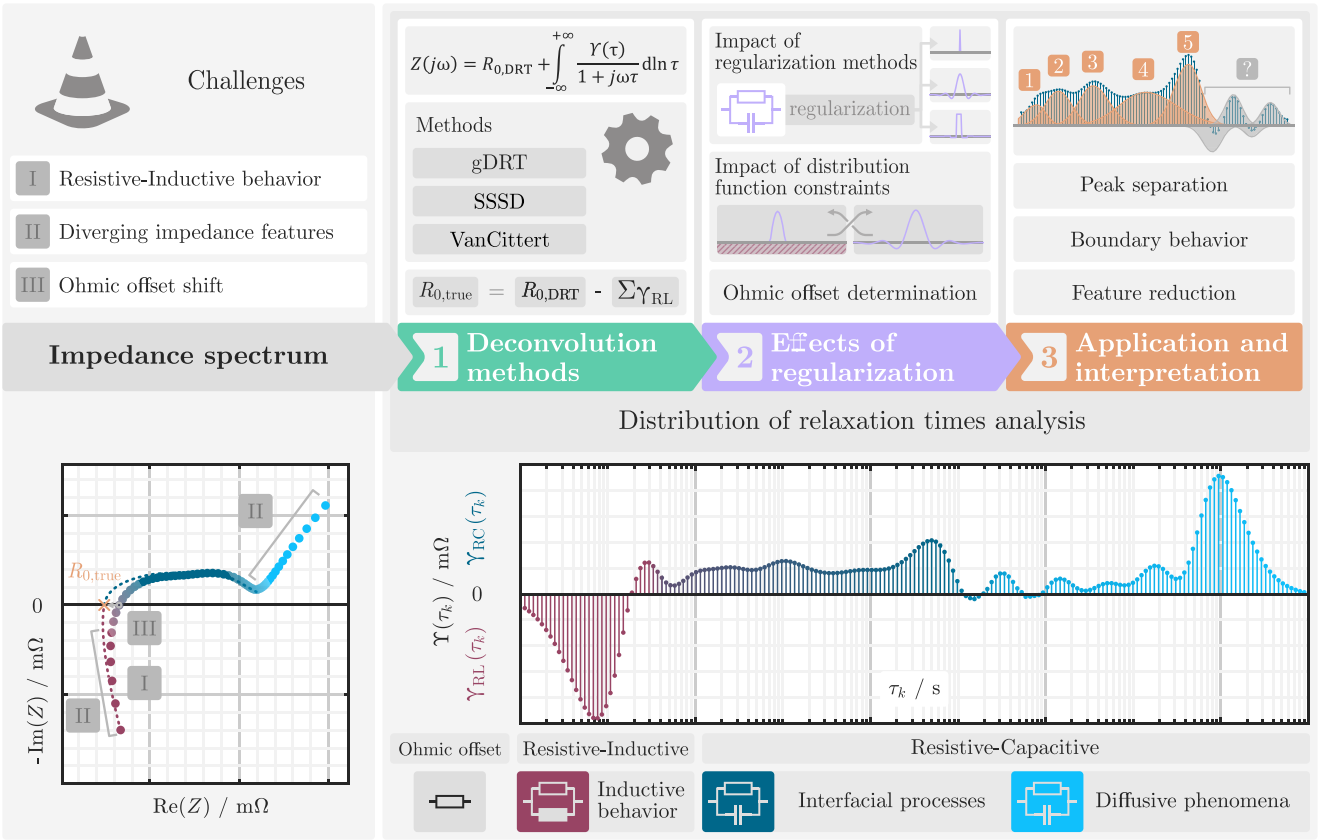

Figure 1. Schematic overview of the three most critical challenges involved in the process of deconvoluting the impedance data into a distribution function. It is exemplarily shown for a li-ion battery spectrum. The analysis is separated in three distinct parts: (1) deconvolution methods, (2) effects of regularization and distribution constraints, and (3) application and interpretation of results. The present publication is focused on the first part.

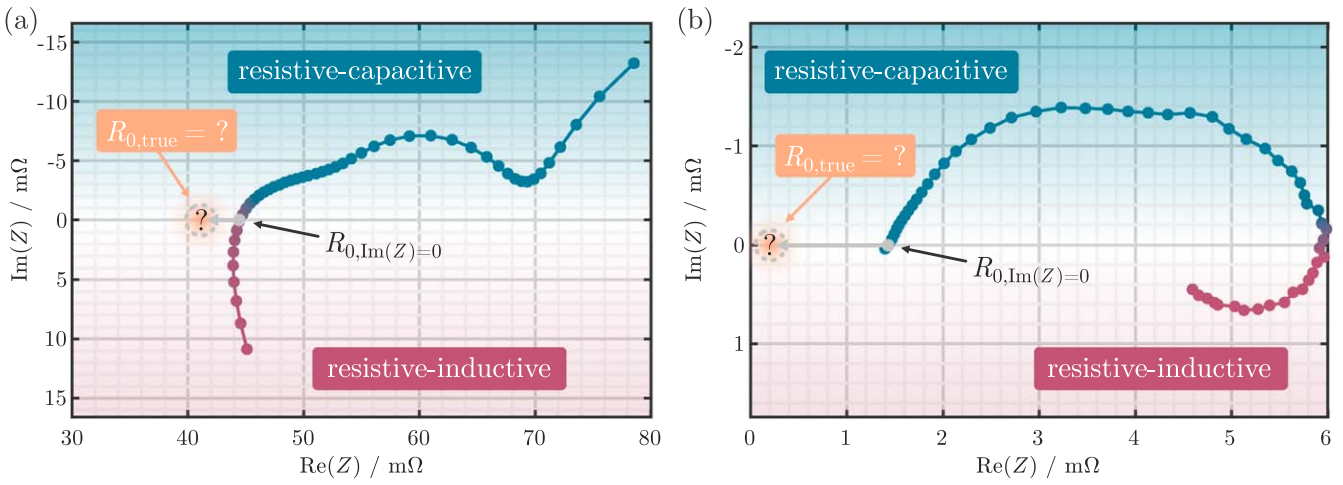

Figure 2. Comparison of two measurement examples with different resistive-inductive features: (a) Li-ion battery with a high and (b) PEM fuel cell with a low frequency inductive contribution. The true ohmic offset of the system $R_{0,\mathrm{true}}$ is different from the zero-crossing resistance $R_{0,\mathrm{Im}(Z)=0}$ and cannot be extracted directly. Information on the two electrochemical systems and their measurement conditions can be found in Table V.

and how exactly a negative distribution function interacts with the algorithm and how it affects the required correction of the ohmic offset needs to be answered.

To evaluate this, three different deconvolution methods are modified to allow for negative polarization in their resulting distribution function. Each algorithm has unique characteristics and capabilities with respect to its type of regularization and mathematical approach (see Table I). The specific selection of different algorithms is intended to demonstrate the general applicability of the proposed changes.

For benchmarking and validation, a known equivalent circuit model is used to provide a synthetic impedance spectrum. The analytical solution for the distribution function is derived based on a novel and efficient transformation relation that does not require prior separation of the real and imaginary parts of the impedance data. In addition to the analytical solution, the result of the electrochemical system analysis (ELSA)[36] is used as a validity indicator. ELSA is a complementary, purely data-driven method that requires no modification or post-processing of its results making a comparison meaningful.

Table I. Comparison and overview of the used DRT methods.

Method	Discretization	Regularization	R_0	Serial lumped elements
gDRT	τ-domain	Tikhonov	✓	✓
VanCittert	τ-domain	Iterations	✓	×
SSSD	τ-domain	Parameter	✓	×
ELSA[36]	—(data-driven)	—	✓	✓

To better understand the implications of negative polarization in the distribution function, a generalized model that can describe both resistive-capacitive and resistive-inductive characteristics is first derived based on the concept of phasances[37] and then used to investigate the interaction with the ohmic offset.

The Generalized Cole-Cole Impedance Model

In the sense of an ECM, a resistive-capacitive process can be understood as a parallel connection of a resistance R and a capacitance C with a distinct time constant $\tau = R \cdot C$. In literature,[3] this is described as the Debye relaxation model with the transfer function

$$Z_{\mathrm{RC}}(j\omega) = \frac{R}{1 + j\omega\tau}. \quad [1]$$

In relation to the underlying physical processes, e.g., the resistance R describes the charge transfer of the active redox reaction occurring at the electrode and the capacitance C the electrochemical double layer forming at the solid–liquid phase boundary. In theory, a double layer at the surface of a solid electrode shows capacitive behavior. Without an ongoing charge-transfer reaction, the transfer function of an ideal capacitance C can be used for description:

$$Z_{\mathrm{C}}(j\omega) = \frac{1}{C(j\omega)}. \quad [2]$$

This is true as long as ideal polarizability can be assumed.[38] In practice, however, a dispersion of capacitance can be observed,[38] leading to a deviation from the ideal resistive-capacitive behavior. In 1941, Cole and Cole[1] studied various dielectric materials and empirically described the electrochemical behavior by adding an exponent φ to $(j\omega)$ in Eqs. 2 and 1. This allows the resistive-capacitive interfacial process at a solid electrode in an electrochemical system to be described by a distribution of polarization over a wide range of time constants instead of a single time constant associated with the Debye model.

The empirical model extended by the exponent φ can be physically understood as a concept of phasance.[37] This allows the formulation of a very general impedance model for non-ideal elements, which can be set up with corresponding value ranges of φ. Applied to Eq. 2, the transfer function of a generalized constant phase element (ϕ element) is given by

$$Z_{\phi}(j\omega, \varphi) = \frac{1}{Q(j\omega)^{\varphi}} \quad [3]$$

and

$$Z_{\mathrm{R}\phi}(j\omega, \varphi) = \frac{R}{1 + (j\omega\tau)^{\varphi}} \quad [4]$$

for the Rϕ element. For any value of φ between 0 and 1, the phasance describes a capacitive or resistive-capacitive behavior, with $\varphi = 1$ representing an ideal process. For this range, Eq. 3 represents a Q element, also known as a CPE element, and Eq. 4 represents an RQ element, also known as a ZARC element or Cole-Cole model. Similarly, values between -1 and 0 describe inductive or resistive-inductive behavior. For this range Eq. 3 represents a K element and Eq. 4 an RK element. While non-ideal RQ elements are commonly discussed, non-ideal inductances K and non-ideal RK elements are yet rarely mentioned in the literature,[39,40] and if so, a physical interpretation is lacking. A detailed overview of the mathematical relations is given in the Table II. In the literature, modified variants of Eq. 4 are sometimes found that have an implicit dependence between the characteristic time constant τ and the exponent φ. With the definitions in Table II, the exponent φ can be changed independently of the polarization and the characteristic time constant. This is illustrated in Fig. 3. It can be seen that a lower value of φ leads to more depressed semicircle, which correlates with a less ideal process. Looking at the imaginary part, it is evident that the characteristic time constant is indeed independent and remains constant.

Table II. Overview of the special cases of the generalized Cole-Cole model and the mathematical relationship of the model parameters. Note that for resistive-inductive models (RL and RK) $L = C^{-1}$ and $K = Q^{-1}$.

$$Z_{\mathrm{R}\phi}(j\omega) = \frac{R}{1 + (j\omega\tau)^{\varphi}}$$

	RC	RQ	RK	RL
φ	1	$0 \leqslant \varphi \leqslant 1$	$-1 \leqslant \varphi \leqslant 0$	-1
τ	$\tau = \sqrt[\varphi]{R \cdot Q}$		$\tau = \sqrt[\varphi]{\frac{K}{R}}$	
C / L	$C = \frac{\tau}{R} = \frac{\sqrt[\varphi]{R \cdot Q}}{R}$		$L = R\tau = R \cdot \sqrt[\varphi]{\frac{K}{R}}$	
Q / K	[-]	$Q = \frac{\tau^{\varphi}}{R}$	$K = R \cdot \tau^{\varphi}$	[-]

The Distribution of Relaxation Times

The distribution of relaxation times method (DRT) requires a transformation from the frequency domain to the τ-domain, resulting in the form of a Fredholm integral of the first kind:[41]

$$Z(j\omega) = \int_0^{\infty} K(j\omega, \tau) \cdot \tilde{\gamma}(\tau)\, \mathrm{d}\tau \quad [5]$$

Here, the kernel function is denoted as $K(j\omega, \tau)$, the resulting impedance function is represented by $Z(j\omega)$, and the distribution function is referred to as $\tilde{\gamma}(\tau)$. For the given problem, the kernel function corresponds to the transfer function of a resistive-capacitive RC element, and the integral boundaries range from the minimum time constant (zero) to infinity. Typically, an ohmic offset is introduced, resulting in

$$Z(j\omega) = R_0 + \int_0^{\infty} \frac{\tilde{\gamma}(\tau)}{1 + j\omega\tau}\, \mathrm{d}\tau = R_0 + \int_{-\infty}^{\infty} \frac{\gamma(\tau)}{1 + j\omega\tau} \mathrm{d}\ln\tau, \quad [6]$$

the well-known form of the DRT, with $\gamma(\tau) = \tau \cdot \tilde{\gamma}(\tau)$.

If the continuous distribution function $\gamma(\tau)$ is treated in the context of a probability distribution, it must remain non-negative. This constraint further supports the physical interpretation, as only positive polarization will be present in the distribution function. However, this restricts the analysis to purely resistive-capacitive spectra, such as those arising from electrical and electrochemical processes, e.g., interfacial resistance, charge transfer, double layer phenomena or diffusion processes. To ensure compliance with the non-negativity constraint of $\gamma(\tau)$, it becomes necessary to remove resistive-inductive effects, as they cannot be represented by the strict definition of the DRT above. As mentioned previously, these effects are often observed in the high frequency region of battery spectra

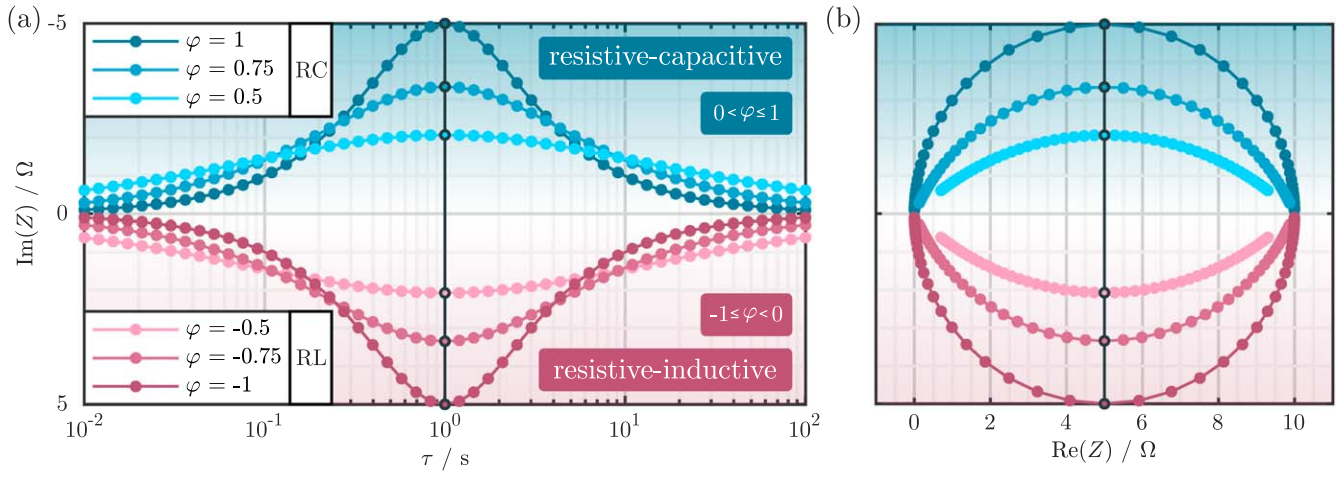

Figure 3. (a) Imaginary part of $R\phi$ elements with different values for the phasor φ. The marked maximum corresponds with the characteristic time constant. (b) Impedance spectra of the analyzed $R\phi$ elements.

and in the low frequency region of fuel cell spectra. Several publications attempt to analyze impedance data by truncating positive imaginary values or disregarding inductive effects,[42–45] which introduces an unquantifiable uncertainty into the analysis. To overcome this limitation, the non-negativity condition for $\gamma(\tau)$ can be dropped in favor of an unconstrained function $\Upsilon(\tau) \in R$, which allows both positive and negative values in the distribution function.

Deconvolution methods.—Since infinite frequencies are experimentally inaccessible and since it is an inverse ill-posed problem for bounded frequencies, the direct evaluation of Eq. 6 for measured impedance spectra is generally not possible. However, there are several classes of methods in the literature that provide approximate solutions for the distribution function. These are based on the Fourier transformation,[46,47] the maximum entropy,[48] and on the discretization of the time constants τ in the integral. The latter includes various algorithms: methods that use the Tikhonov regularization,[28,49] the separated sparse spike deconvolution,[50] and the iterative Van Cittert algorithm.[50] All of these share a common characteristic: they provide an approximate solution for the distribution function even in the absence of a closed-form analytical expression for the impedance. In this article, methods based on the integral discretization are used. To derive numerical approaches for these, the Fredholm integral Eq. 6 must first be discretized in terms of frequencies and time constants.

To do so, the continuous expression for impedance in Eq. 6 is replaced by a discrete set of equations for the N_f measured frequencies. At the same time, the continuous distribution function $\gamma(\tau)$ is discretized in N_τ steps. Both approximations, together with the selected kernel function, transform the continuous Fredholm integral into a discrete system of equations. To obtain a set of real-valued equations, assuming a real-valued distribution function, the real and imaginary parts can be separated, leading to

$$\begin{aligned} Z(j\omega) &= R_0 + \int_{-\infty}^{\infty} \frac{\Upsilon(\tau)}{1 + j\omega\tau} \mathrm{d}\ln\tau \\ &\approx R_0 + \sum_{k=1}^{N_\tau} \left(\frac{1}{1 + (\omega\tau_k)^2} - j\frac{\omega\tau_k}{1 + (\omega\tau_k)^2} \right) \Upsilon_k. \end{aligned} \quad [7]$$

The expression can be written compactly in the matrix vector form

$$\mathbf{Z} = \begin{bmatrix} \mathbf{Z}_{\mathrm{re}} \\ \mathbf{Z}_{\mathrm{im}} \end{bmatrix} = R_0 \cdot \mathbf{1} + \underbrace{\begin{bmatrix} \mathbf{A}_{\mathrm{re}} \\ \mathbf{A}_{\mathrm{im}} \end{bmatrix}}_{=\mathbf{A}} \boldsymbol{\Upsilon}, \quad [8]$$

with $\mathbf{A}_{\mathrm{re}}, \mathbf{A}_{\mathrm{im}} \in \mathbb{R}^{N_f} \times N_\tau$, $\mathbf{Z}_{\mathrm{re}} = \left[Z_{\mathrm{re}}(j\omega_1) \cdots Z_{\mathrm{re}}(j\omega_m) \cdots Z_{\mathrm{re}}(j\omega_{N_f}) \right]^{\mathrm{T}}$, $\mathbf{Z}_{\mathrm{im}} = \left[Z_{\mathrm{im}}(j\omega_1) \cdots Z_{\mathrm{im}}(j\omega_m) \cdots Z_{\mathrm{im}}(j\omega_{N_f}) \right]^{\mathrm{T}}$ and $\boldsymbol{\Upsilon} \in \mathbb{R}^{N_\tau \times 1}$. To calculate Υ from $\mathbf{Z}$, it is necessary to determine $\mathbf{A}_{\mathrm{re}}^{-1}$ and $\mathbf{A}_{\mathrm{im}}^{-1}$. Unfortunately, the determinants are nearly singular leading to an ill-conditioned matrix A: $|\mathbf{A}_{\mathrm{re}}| \approx 0$ and $|\mathbf{A}_{\mathrm{im}}| \approx 0$. Therefore, the equation is not directly numerically solvable for Υ.

Analytical solution.—If a mathematical expression is available, a continuous analytical solution for the distribution function can be found by directly solving the integral equation. For a known closed-form analytical impedance transfer function, the corresponding distribution function can be computed by various methods. As early as 1941, Fuoss and Kirkwood[51] presented a transformation that evaluates the analytic real and imaginary parts of the transfer function, which is still a popular approach today.

Rosenberg[52] showed a method similar to that used by Fuoss and Kirkwood.[51] After small changes in his approach, it can be seen that the distribution of relaxation times can be calculated analytically by replacing $j\omega$ in $Z(j\omega)$ with $\frac{1}{\tau} \cdot e^{\pm j\pi}$:

$$\gamma(\tau) = \frac{j}{2\pi} \cdot \left(Z\left(\frac{1}{\tau} \cdot e^{j\pi} \right) - Z\left(\frac{1}{\tau} \cdot e^{-j\pi} \right) \right) \quad [9]$$

Note that Eq. 9 will only yield a real-valued distribution $\gamma(\tau)$ if the impedance function $Z(j\omega)$ can be represented by the kernel function selected in Eq. 6. Details can be found in Appendix C. The advantage of this transformation is that it does not require a separation of the real and imaginary parts, which simplifies the analytical solution. However, both transformations lead to the same distribution function. Inserting the generalized phasance transfer function Eq. 4 into the transformation Eq. 9 yields the distribution function

$$\Upsilon_{\mathrm{R}\phi}(\tau, \varphi) = \frac{R}{2\pi} \frac{\sin(\varphi\pi)}{\cosh(\varphi[\ln(\tau_{\mathrm{R}\phi}) - \ln(\tau)]) + \cos(\varphi\pi)}. \quad [10]$$

Analogous to the effect of φ on the impedance, the value of φ determines the type of element. Note that the solution is only valid for $0 < \varphi < 1$ and $-1 < \varphi < 0$. For ideal elements with $|\varphi| = 1$ the distribution function must be simplified to scaled Dirac impulses.

Separated-sparse-spike deconvolution.—The SSSD method is a modified version of the sparse spike deconvolution, which is a signal processing technique used in seismic data analysis.[53] The method

tries to find isolated sharp peaks in the signal. In Ref,[50] the algorithm is described in detail. However, the minimization equation was slightly modified to

$$\min_{0<\varphi<1}\left(||\mathbf{Z}_{\text{im}}-\mathbf{A}_{\text{im}}\cdot\mathbf{G}(\boldsymbol{\varphi})\cdot\mathbf{c}||_2+||\mathbf{Z}_{\text{re}}-\mathbf{A}_{\text{re}}\cdot\mathbf{G}(\boldsymbol{\varphi})\cdot\mathbf{c}||_2+\frac{||\sqrt{\ln(1+\boldsymbol{\varphi})}||_2}{\lambda_S}\cdot\sqrt{N_f}\cdot\overline{\mathbf{Z}_{\text{re}}}\right). \quad [11]$$

In contrast to other regularization methods that typically use the norm of $\mathbf{Z}$, the SSSD method uses a sparse vector $\boldsymbol{\varphi}$ for the regularization. An issue that arises is that φ is nearly independent of the magnitude and the resolution of the spectra. Therefore it should be scaled with the mean $\overline{\mathbf{Z}}_{\text{re}}$ and the number of data points $\sqrt{N_f}$. A suitable regularization parameter λ_S was empirically determined to be approximately 3000.

The vector $\mathbf{c}$ is calculated in each iteration by

$$\min_{\mathbf{c}}(||\mathbf{Z}_{\text{re}}-\mathbf{A}_{\text{re}}\cdot\mathbf{G}(\boldsymbol{\varphi})\cdot\mathbf{c}||_2). \quad [12]$$

By adding the condition $\mathbf{c}\geqslant 0$, the distribution function will be positive. After the minimization, it is obtained by

$$\boldsymbol{\Upsilon}=\mathbf{G}(\boldsymbol{\varphi})\cdot\mathbf{c} \quad [13]$$

which can afterwards be used to find the ohmic offset R_0 by solving the optimization problem

$$\min_{R_0}(||\mathbf{Z}_{\text{re}}-R_0\cdot\mathbf{1}-\mathbf{A}_{\text{re}}\cdot\boldsymbol{\Upsilon}||_2). \quad [14]$$

Van-cittert-/gold-algorithm.—In Ref,[50] it can be seen that the Gold algorithm, a modified version of the Van-Cittert algorithm, gave good results in determining a positive DRT. It is now used to determine the unconstrained distribution function Υ. The algorithm is iterative and its extent of regularization depends on the iterations n. First, the distribution function is determined separately for the real and imaginary parts. The solution for the real part is calculated with

$$\boldsymbol{\Upsilon}_{1,n+1}=\boldsymbol{\Upsilon}_{1,n}+\mu_1(\mathbf{A}_{\text{re}}^T\mathbf{Z}_{\text{re}}-\mathbf{A}_{\text{re}}^T\mathbf{A}_{\text{re}}\boldsymbol{\Upsilon}_{1,n}) \quad [15]$$

and $\mu_1=\frac{1}{||\mathbf{A}_{\text{re}}||_2}$ and the solution for the imaginary part with

$$\boldsymbol{\Upsilon}_{2,n+1}=\boldsymbol{\Upsilon}_{2,n}+\mu_2(\mathbf{A}_{\text{im}}^T\mathbf{Z}_{\text{im}}-\mathbf{A}_{\text{im}}^T\mathbf{A}_{\text{im}}\boldsymbol{\Upsilon}_{2,n}) \quad [16]$$

and $\mu_2=\frac{1}{||\mathbf{A}_{\text{im}}||_2}$.

To determine the number of iterations required to achieve optimal regularization, a similar technique described by Nicolas et al.[54] is applied. In contrast to their proposed method, which requires two spectra, only the imaginary part and the real part are used to find the best iteration number n_{opt} by minimizing

$$\min_n||\boldsymbol{\Upsilon}_{1,n}-\boldsymbol{\Upsilon}_{2,n}||_2. \quad [17]$$

This method depends on good preprocessing. An incorrectly determined resistance R_0 causes a shift in the real axis and therefore an additional peak in Υ_1. To eliminate this dependence, the real part used in Eq. 15 is replaced according to the derivation shown in the Appendix D, giving

$$\boldsymbol{\Upsilon}_{1,n+1}=\boldsymbol{\Upsilon}_{1,n}+\mu_1(\mathbf{A}_{\text{re}}'^T\mathbf{Z}_{\text{re}}'-\mathbf{A}_{\text{re}}'^T\mathbf{A}_{\text{re}}'\boldsymbol{\Upsilon}_{1,n}) \quad [18]$$

with $\mu_1=\frac{1}{||\mathbf{A}_{\text{re}}'||_2}$.

After finding the optimal number of iterations n_{opt} with Eq. 17, the final distribution function is computed by using the real and imaginary parts simultaneously in

$$\boldsymbol{\Upsilon}_{n+1}=\boldsymbol{\Upsilon}_n+\frac{\mu_1}{2}(\mathbf{A}_{\text{re}}'^T\mathbf{Z}_{\text{re}}'-\mathbf{A}_{\text{re}}'^T\mathbf{A}_{\text{re}}'\boldsymbol{\Upsilon}_n)+\frac{\mu_2}{2}(\mathbf{A}_{\text{im}}^T\mathbf{Z}_{\text{im}}-\mathbf{A}_{\text{im}}^T\mathbf{A}_{\text{im}}\boldsymbol{\Upsilon}_n) \quad [19]$$

until $n=n_{\text{opt}}$. The same optimization problem as for the SSSD in Eq. 14 is used to determine the ohmic offset R_0.

Generalized distribution of relaxation times method.—In this approach, the underlying Fredholm integral, as shown in Eq. 7, is discretized into a sum of RC elements, representing a Voigt network. Each element has a unique time constant τ_k and a corresponding polarization $\gamma(\tau_k)$. The time constants must be predefined with a logarithmic spacing, while the frequencies are given by the experiment. The number of time constants is independent of the frequencies, but it is recommended to use a larger number of time constants and to extend their range by at least one decade. This helps to minimize boundary effects in the distribution function.[41]

As shown in Eq. 8, this results in a system of real-valued linear equations. The inverse problem is ill-posed and the system matrices are ill-conditioned, which requires the use of a regularization technique. For this purpose, the Tikhonov L2 regularization is most commonly used. The regularization parameter λ_G can be selected using the real-imaginary cross-validation (RICV) method,[55] the L-curve method,[49] or other comparable techniques.[41] In this study, the Tikhonov regularization in combination with the L-curve method is used.

With the extended DRT (eDRT), Hahn et al.[14] took this idea forward to cover non-distributed capacitive and inductive features in the spectrum by adding lumped serial elements to the Voigt network. For a more general approach, Danzer[28] proposes the generalized DRT (gDRT) with the addition of a second distribution function that includes the kernel function of an RL element to allow the analysis of any spectrum exhibiting resistive-inductive behavior. However, this increases the size of the equation system.

To address this disadvantage, the second distribution function can be replaced with a single unconstrained distribution function. The resulting size and structure of the matrices and vectors can be found in Ref.[41]. This reformulation leads to a more compact and efficient minimization problem

$$\min_{\boldsymbol{\Upsilon}_G\in\mathbb{R}}(||\mathbf{A}_G\boldsymbol{\Upsilon}_G-\mathbf{Z}||_2+||\lambda_G\boldsymbol{\Upsilon}_G||_2) \quad [20]$$

to be solved. The optimized vector $\boldsymbol{\Upsilon}_G=\begin{bmatrix}\boldsymbol{\Upsilon} & R_0 & C_0 & L_0\end{bmatrix}^T$ inherits the distribution function Υ and the parameters of the lumped serial elements R_0, C_0 and L_0. Without the use of regularization, the concept is identical to that of the extended Kramers-Kronig test, which is commonly used to validate impedance data.[56]

Interpretation of a negative distribution function.—Both resistive-capacitive and resistive-inductive characteristics can be modeled with the same kernel function by substituting the resistive-inductive element with a resistive-capacitive element, which has a negative phasor φ. It can be represented as a negative resistive-capacitive element with an ohmic shift. This can be demonstrated as follows (full derivation in the Appendix A):

$$\begin{aligned}Z_{R\phi}(-R,\varphi,\tau,j\omega)+\Theta&\overset{!}{=}Z_{R\phi}(R,-\varphi,\tau,j\omega)\\ \frac{-R}{1+(j\omega\tau)^{\varphi}}+\Theta&=\frac{R\cdot(j\omega\tau)^{\varphi}}{1+(j\omega\tau)^{\varphi}}\\ \Leftrightarrow\Theta&=R\end{aligned} \quad [21]$$

Instead of having two separate distribution functions for resistive-capacitive and resistive-inductive elements, they are now superimposed into

$$\Upsilon(\tau) = \gamma_{\mathrm{RC}}(\tau) - \gamma_{\mathrm{RL}}(\tau). \quad [22]$$

With this and the substitution shown in Eq. 21 the Fredholm integral of the DRT (see Eq. 6) transforms according to the Appendix B into

$$Z(j\omega) = R_{0,\mathrm{true}} + \int_{-\infty}^{\infty} \frac{\Upsilon}{1 + j\omega\tau} \, \mathrm{d}\ln\tau + \int_{-\infty}^{\infty} \gamma_{\mathrm{RL}} \, \mathrm{d}\ln\tau. \quad [23]$$

The integral of the distribution function γ_{RL}, which characterizes the resistive-inductive elements, now adds an extra contribution to the ohmic offset. To derive a discretized form of Eq. 23 two discretization steps are required: First, the integral is transformed into a discrete series of time constants, and second, the continuous functions for frequency and impedance are replaced by its corresponding discrete measurement samples, resulting in

$$Z(j\omega_m) = \underbrace{R_{0,\mathrm{true}} + \sum_{k=1}^{N_\tau} \gamma_{\mathrm{RL},k}}_{\triangleq R_{0,\mathrm{DRT}}} + \sum_{k=1}^{N_\tau} \frac{\Upsilon_k}{1 + j\omega_m\tau_k}. \quad [24]$$

In order to recover the true ohmic offset $R_{0,\mathrm{true}}$, the ohmic offset $R_{0,\mathrm{DRT}}$ obtained by the DRT must be corrected with the polarization of the resistive-inductive distribution function. The same applies to the calculation of the total resistive-capacitive polarization. For this, the superimposed and unconstrained distribution function Υ must be separated into both polarization types

$$\begin{aligned} \sum_{k=1}^{N_\tau} \Upsilon(\tau_k) &= \sum_{k=1}^{N_\tau} \Upsilon_{\Upsilon>0}(\tau_k) - \sum_{k=1}^{N_\tau} |\Upsilon_{\Upsilon<0}(\tau_k)| \\ &= \sum_{k=1}^{N_\tau} \gamma_{\mathrm{RC},k} - \sum_{k=1}^{N_\tau} \gamma_{\mathrm{RL},k}, \end{aligned} \quad [25]$$

where negative values are assigned to resistive-inductive and positive to resistive-capacitive polarization.

The same concept can be applied if the primary kernel is based on the transfer function of a resistive-inductive element instead. However, this does not change the fundamental implications, and since resistive-capacitive processes are the primary mechanism in electrochemical systems, this approach will not be explored further.

Effect on the ohmic offset.—The ohmic resistance is a frequently studied key characteristic of electrochemical systems. However, this parameter is not always directly accessible, particularly when inductive or resistive-inductive characteristics are present within the spectrum. As shown in Fig. 4, there are two conceivable variants of how a resistive-inductive feature can interact with a resistive-capacitive feature, depending on the relative location of the characteristic time constants. This is visualized using a novel approach: to show the local frequency-dependent contribution of a selected impedance component to the overall impedance response, a weighting metric is calculated. This metric reflects how the shape of the impedance curve changes as the selected component is removed from the overall spectrum in frequency increments. It is determined from a combination of the rate of change of the modulus of the local deviation between the full and modified spectrum and the rate of change of the modulus of the selected impedance component itself. Thick lines indicate regions where the selected element has a pronounced effect on the spectrum. Importantly, this approach does not represent a physical removal of circuit elements such as RC or RL pairs. Instead, it quantifies the contribution of the selected component to the composite spectrum based on simulated incremental subtraction and modulus deviation. A comparably slow resistive-inductive process appears at low frequencies, while a faster process appears at high frequencies. A slow resistive-inductive process with a large time constant, adds its entire polarization to the zero-crossing resistance. In the other case, the zero-crossing is only partially shifted, depending on the overlap and the polarization ratio of the opposing processes. A relatively high resistive-inductive polarization and a large overlap will induce a larger shift than vice versa. This can be mathematically expressed by separately analyzing and combining the resistive-capacitive case ($\varphi > 0$) and the resistive-inductive case ($\varphi < 0$) of Eq. 4:

$$Z(j\omega \to 0) = R_{0,\mathrm{true}} + \sum_{k=1}^{N_\tau} \gamma_{\mathrm{RC},k} \quad [26]$$

$$Z(j\omega \to \infty) = R_{0,\mathrm{true}} + \sum_{k=1}^{N_\tau} \gamma_{\mathrm{RL},k} \quad [27]$$

In such instances, relying on the zero-crossing resistance yields an erroneous value and requires the use of an advanced analysis method, i.e., the DRT with an unconstrained distribution function to capture both polarization types.

However, according to Eq. 24, it is necessary to correct the obtained ohmic resistance from the DRT analysis by subtracting the negative polarization

$$R_{0,\mathrm{true}} = R_{0,\mathrm{DRT}} - \sum_{k=1}^{N_\tau} |\Upsilon_{\Upsilon<0}(\tau_k)|. \quad [28]$$

Results

In this section, the three previously introduced algorithms for solving the discretized problem of the distribution of relaxation times analysis are employed to calculate the distribution function without the non-negativity constraint. The concept of the proposed method is proven by applying it to the impedance spectrum of a synthetically designed equivalent circuit model. Figure 5 illustrates the synthetic impedance spectrum of the equivalent circuit model designed. The model parameters and frequency information are presented in detail in Table III, located in Sect. 6. The model has been constructed with the specific intention of serving as a proof of concept for the proposed DRT methods. It contains a serial ohmic resistor, a non-ideal RK element, and a non-ideal RQ element, where each element has its maximum impact on the total impedance within a specific frequency range. For enhanced visual comprehension, the effective frequency range of each element is indicated by thickness and color saturation. The higher the intensity of the marking, the more significant the impact of the element at that frequency. The time constants of the RK element and the RQ element are selected far apart from each other to reduce the overlap. As a result, there is only a minimal local effect in the range of 1.9 kHz from either the RK element or the RQ element, meaning that the course of the impedance remains largely unchanged if one of the elements is removed from the model. Without a pronounced overlap, the impact on the ohmic offset is minimized, allowing for validation of the theoretically derived relationship between the unconstrained distribution function and the ohmic offset. This difference can be quantified by superimposing the analytical distribution functions (see Eq. 10) of the two elements. As shown in Fig. 6, the distributed polarization of the non-ideal elements leads to an overlap of both functions, which reduces the effective resistive-capacitive and resistive-inductive polarizations and converts the difference into an additional ohmic contribution. This effect occurs in addition to the zero-crossing shift described in Fig. 4. Both effects can be observed as a superposition in the given example. However, only the zero-crossing shift is theoretically recoverable. Therefore, the results of any DRT method are expected to align with the effective polarizations according to Table IV rather than with the true parameters of the ECM model. More significant overlapping spectra and their implications will be investigated in subsequent publications.

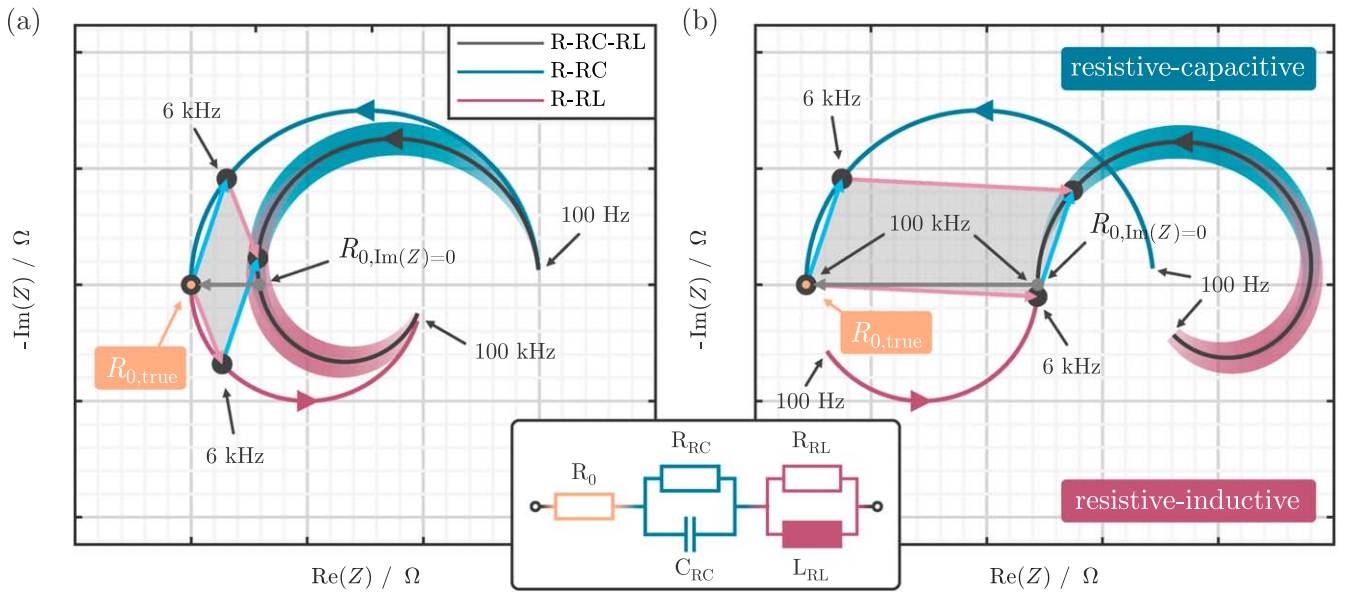

Figure 4. The figure shows the impedance for an ECM consisting of an ohmic resistor, an RC and an RL element. Depending on the position of the time constant of the RL element, the superposition of the two elements is different. The spectrum in (a) represents a high frequency and the spectrum in (b) represents a low frequency RL element. The superposition can be visualized geometrically and is shown exemplarily for the frequency point at 6 kHz. The frequency-specific relevance of the impedance of a single element in the superimposed spectrum is emphasized by its line thickness. Thick lines indicate a high influence in this frequency range.

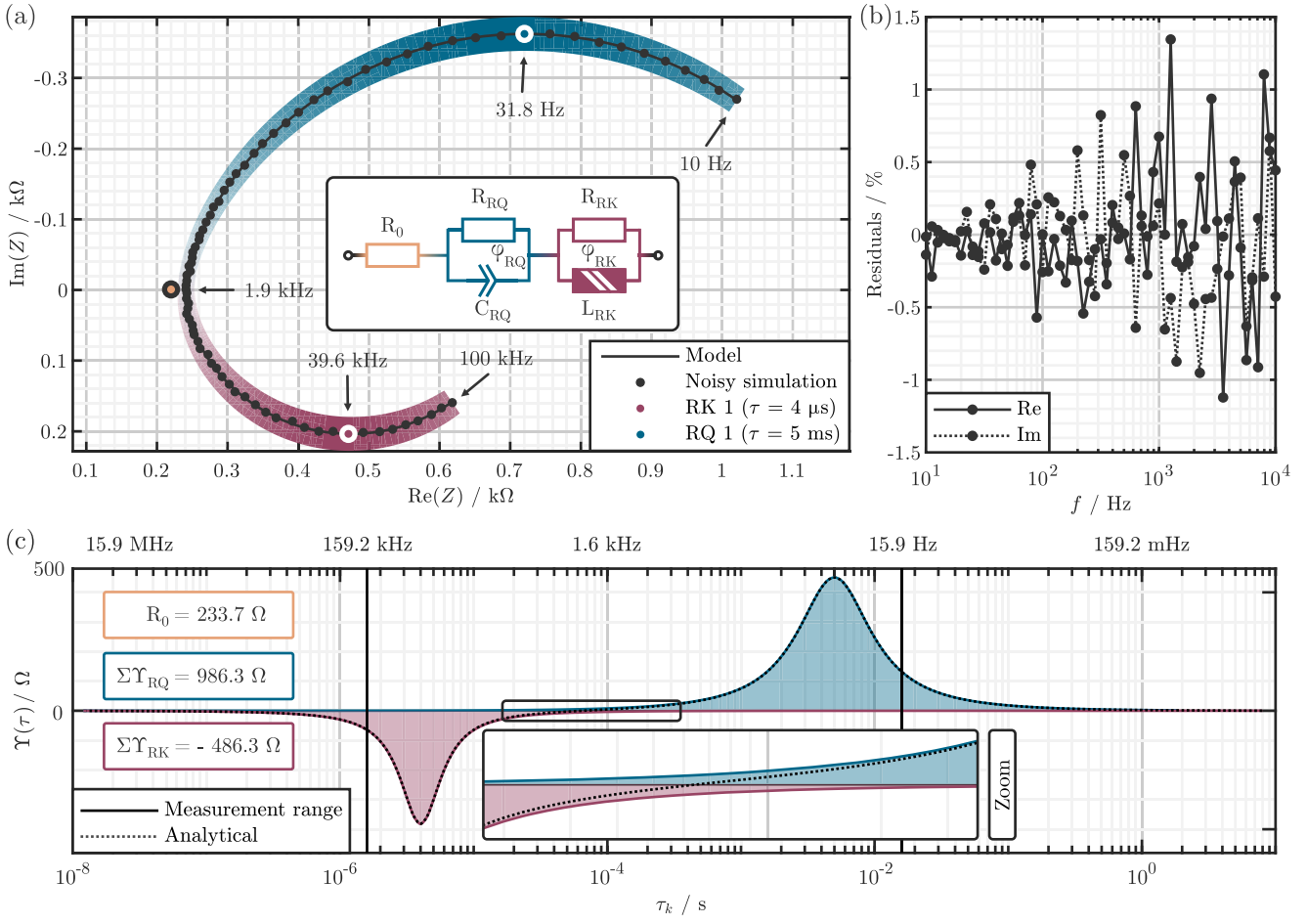

Figure 5. (a) Impedance spectra of the ECM model with and without superimposed noise. The frequency-specific relevance of the impedance of a single element in the superimposed spectrum is emphasized by its line thickness. Thick lines indicate a high influence in this frequency range. (b) Residuals of the simulation including noise with a relative error of ≈1%. (c) Analytic solution for the overlapping distribution functions of both elements with the superimposed effective polarization and the increased ohmic offset. *Note*: The analytic distribution function shown in (c) is a continuous solution. The quantitative polarization cannot be compared directly with a discrete distribution function.

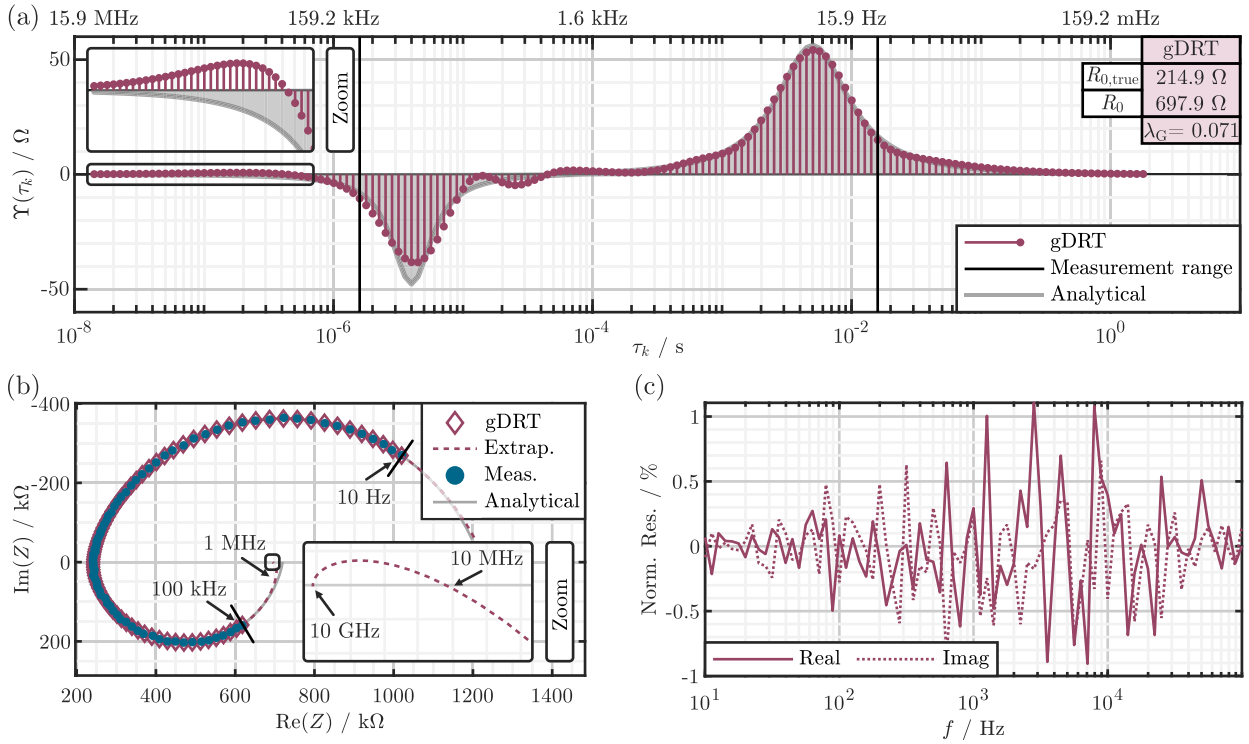

Figure 6. (a) Distribution function of the impedance spectrum for the synthetic equivalent circuit model, calculated using the gDRT method. The black distribution represents the superposition of the two shaded distributions, which correspond to the analytical solution for each element. (b) Reconstructed impedance, including simulated interpolation between frequency points and simulated extrapolation at both boundaries by one decade. (c) Normalized relative residuals between the DRT reconstruction and measurement. *Note*: The analytic distribution is presented as a continuous line for visual reasons. The values are only valid at the discrete time constants τ_k.

Table III. Model parameters used for the equivalent circuit model.

	$\mathbf{R}_0$	RK	RQ
R	220 Ω	500 Ω	1000 Ω
τ	—	4 μs	5 ms
C/L	—	2.0 mH	5.0 μF
φ	—	0.88	0.80

As a detailed example, the results of the gDRT method are shown in Fig. 6 and compared to the analytical solution. Due to the selected synthetic model the gDRT is configured without an inductive or capacitive serial lumped element and the regularization parameter λ_G is determined using the L-curve method. The overall shape of the distribution function is in good agreement with the analytical solution. The position of the peaks, or rather their time constants, align well with the model values. Slight deviations in height and shape can be observed, with larger discrepancies for the RK element compared to the RQ element. This is attributed to the higher exponent φ_{RK}, which corresponds to a sharper and therefore more ideal characteristic. The applied Tikhonov regularization is known to increase the smoothing and introduce more oscillations for sharper peaks.[41] With 698Ω, the ohmic resistance obtained from the gDRT is higher than the anticipated resistance of 234Ω. However, this difference is expected when using an unconstrained distribution function to simulate resistive-inductive characteristics. According to Eq. 28, it can be corrected by removing the resistive-inductive polarization from the obtained ohmic offset. This results in a value of 215Ω, which is lower than the analytically derived 234Ω. The difference is due to the interaction between the Tikhonov regularization and the characteristic time constant of the RK element. In the magnified Section of Fig. 6(a), the time constant range extends beyond the lower limit of the measurement range and shows a positive polarization contribution. Due to the distant time constants, the resulting impedance manifests itself as a purely ohmic shift within the measurement range. Consequently, its contribution has no effect on the residuals, and without the penalty term of the Tikhonov L2 regularization, the polarization of the lower extension can no longer be uniquely distinguished from the lumped series resistance. However, the inclusion of the penalty term constrains this domain to minimize the L2 norm, ultimately causing the observed overshoot and reduced ohmic resistance. This is further confirmed by high-frequency extrapolation of the simulated impedance, where the overshoot produces an additional high-frequency resistive-capacitive contribution. Considering the polarization of the Section of 13.2Ω, the obtained ohmic resistance differs from the analytical value by −2.6% and without by −8.2%.

The results of the remaining methods are presented and compared both visually with the analytical and purely data-driven ELSA solution[36] in Fig. 7, and quantitatively in Table IV. All distribution functions obtained show good agreement with the analytical solution. It should be noted that the following comparison is not intended to determine which method works best for this specifically selected impedance spectrum, but rather to evaluate whether the proposed modification produces valid results.

Among the methods tested, the SSSD algorithm comes closest to the true solution in terms of shape, process polarization, and ohmic offset, with a relative error of less than 0.9%. The distribution function has no visual oscillations and avoids overshooting in the high frequency range, unlike the gDRT method or the VanCittert algorithm.

The VanCittert algorithm behaves more like the gDRT method, with visible oscillations and more smoothed peaks. Interestingly, the distribution function shows a qualitatively identical overshoot in the high frequency range, but with a lower polarization of 5.9Ω. Adding

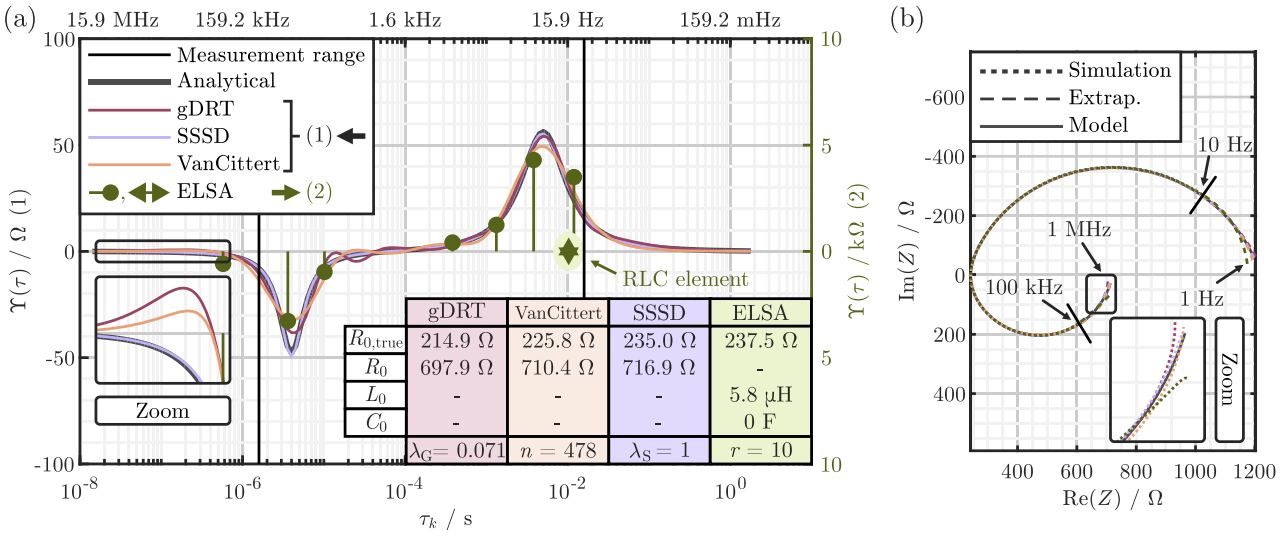

Figure 7. (a) Comparison of the analytically calculated distribution function with the results of the gDRT, VanCittert and SSSD methods. The calculated ohmic offset R_0, the corrected true ohmic offset $R_{0,\mathrm{true}}$ and the meta-parameters of the methods are shown in tabular form. (a) Comparison of the simulated and extrapolated impedance of the model and the gDRT, VanCittert and SSSD methods. *Note*: The distribution is presented as a continuous line for visual reasons. The values are only valid at the discrete time constants τ_k.

Table IV. Comparison of the true model parameters and the parameters calculated by the gDRT, VanCittert, and SSSD methods. R_0 is the resistance obtained directly by the methods, $R_{0,\mathrm{true}}$.

	Model	Analytical	gDRT	VanCittert	SSSD	ELSA
$R_{0,\mathrm{true}}$	220Ω	234Ω	215Ω	226Ω	235Ω	238Ω
R_0	—	—	698Ω	710Ω	717Ω	—
$\Sigma\Upsilon_{\mathrm{RL}}$	−500Ω	−486Ω	−483Ω	−485Ω	−482Ω	−483Ω
$\Sigma\Upsilon_{\mathrm{RC}}$	1000Ω	986Ω	1013Ω	977Ω	982Ω	946Ω

Table V. Information on test objects, operating conditions, measurement equipment, and conditions as well as references.

	Lithium-ion battery	Synthetic Model	PEM fuel cell
Technology details	A123 Systems, 26650 lithium iron phosphate—graphite, 2.5 A h	R-RK-RQ	ElringKlinger single PEM fuel cell, active surface area 50 cm^2
Operating point	50% state of charge, 3.27 V, 20 °C	—	1A, relative humidity of 83.4%, stoichiometry of 4.0/2.0
Measurement device	Zahner Zennium Pro	—	Scribner Associates fuel cell test station with 885 Fuel Cell Potentiostat
EIS mode	galvanostatic	—	galvanostatic
Amplitude	30 mA	—	100 mA
Min. frequency	52 mHz	10 Hz	10 mHz
Max. frequency	17 kHz	100 kHz	3981 Hz
No. of frequencies	49	81	57
Reference	Danzer[28]	—	Pivac et al.[57]

this additional polarization to the ohmic resistance, the total is 231.7Ω, which corresponds to a relative error of 1%.

In terms of total resistive-capacitive polarization, the gDRT method overestimates it by 13.8Ω (1.4%), while the VanCittert algorithm underestimates it by −14.9Ω (−1.5%). This difference is visually apparent in the low-frequency impedance extrapolation, where the gDRT semicircle appears slightly larger and the VanCittert semicircle appears slightly smaller. In contrast, the SSSD algorithm performs best, with a deviation of only −4Ω (−0.4%). For the total resistive-inductive polarization, the differences between the methods are relatively small, with a maximum deviation of 0.8%, making them very comparable in this aspect.

The ELSA method aims to identify a minimum-order system that accurately describes the data. While the other deconvolution methods lead to a model order of 164, ELSA achieves a significantly lower model order of 10. Due to this structural difference, a direct comparison with the analytical solution is not straightforward, as it consists of single separated peaks. What can be seen is that the envelope of the peaks closely follows the shape of the analytical solution. The overall polarization of the resistive-inductive peaks is comparable to the other methods. In the case of resistive-capacitive polarization, the difference is −40Ω (−4%). A possible explanation for the higher deviation is that ELSA, as a purely data-driven method, has no regularization technique to smooth the solution.

Without this, it is not able to reconstruct or approximate the missing polarization of the distributed process beyond the lower measurement frequency. However, much more interesting is the determined ohmic offset: With an error of 4Ω (1.7%), it confirms the expectation of the analytical solution and shows that the ohmic offset correction works correctly for the other methods.

Conclusions

The distribution of relaxation times (DRT) method represents an effective approach for analyzing electrochemical impedance spectra. By transforming the data into the domain of time constants, the separability of peaks can be enhanced without the necessity of *a priori* understanding of the occurring processes, allowing for a more comprehensive insight. It is therefore the preferred method for identifying and characterizing features within an electrochemical impedance spectrum and attributing them to underlying physicochemical processes. However, the impedance spectra of many electrochemical systems, especially those of lithium-ion batteries, electrolyzers, and fuel cells, are rather intricate. In addition to an ohmic offset (R) and resistive-capacitive (RC) characteristics, they also comprise resistive-inductive (RL), inductive (L), and capacitive (C) characteristics.

In this study, the concept of phasances is adapted to extend the deconvolution method of the DRT by allowing the use of a negative distribution function to simultaneously capture both resistive-inductive and resistive-capacitive characteristics within a single distribution function. The general applicability is demonstrated using three different algorithms: the generalized DRT, the VanCittert algorithm, and the Separated Sparse Spike Deconvolution method. Each algorithm uses a unique computational approach to solve the underlying Fredholm integral equation of the DRT analysis. The modification is validated by comparing the computational results with an analytically derived solution of an equivalent circuit model. An efficient transformation is used for this step, which does not require a prior separation of the transfer function into its real and imaginary parts.

The results confirm that it is feasible to successfully remove the non-negativity constraint traditionally imposed on the distribution function to capture resistive-inductive behavior. However, this change requires additional considerations for determining the ohmic offset. For an electrochemical system, the observed zero-crossing resistance typically deviates from the true ohmic offset due to overlapping resistive-inductive and resistive-capacitive characteristics, causing an increase in resistance as well as a visual shift. The presented modified DRT approach helps to determine the true ohmic offset. However, due to the removal of the non-negativity constraint, the resulting ohmic offset from the analysis is a superposition of the true ohmic offset and the sum of the negative polarization and must be corrected. The resulting ohmic offset of all three modified deconvolution methods falls within the range of the expected analytical value and thus proves the correction approach. This is further supported by the result of the purely data-driven and unmodified ELSA method.

By removing the non-negativity constraint on the distribution function and applying the post-processing step to the ohmic offset, the first part of the challenge of analyzing spectra containing both resistive-inductive and resistive-capacitive characteristics is met. This provides significant advantages for subsequent analyses that rely on the determined resistance, as it eliminates the need for prior data truncation, which would result in a distorted distribution function and incorrect ohmic offset.

However, the discussion of the results suggests that there are other influences that affect the successful and reliable interpretation of the results of the DRT analysis. The removal of the non-negativity constraint interacts with the regularization technique, leading to ambiguities in the boundary regions and different peak shapes with an increased tendency to show oscillations. This complicates the process and leads to additional challenges that will be addressed in the following parts.

Experimental

The equivalent circuit model used consists of one ideal resistance R, one non-ideal RL process R_K, and one non-ideal RC processes R_Q. The time constant of the RL process is selected with the intention of avoiding an overlapping RL/RC behavior in the spectrum by placing it in a different order of magnitude from the time constant of the RC processes. Without a pronounced overlap, the impact on the true ohmic offset is minimized, allowing for validation of the theoretically derived relationship between the unconstrained distribution function and the ohmic offset.

In order to simulate real-world measurement conditions, a complex Gaussian white noise was applied to the synthetic impedance data. The magnitude was chosen to give a relative error of approximately 1% in the residuals, and the frequency ranges from 100 kHz to 10 Hz, with 20 steps per decade. The model parameters are listed in Table III.

Details on the in Fig. 2 presented experimental impedance data can be found in Table V.

Acknowledgments

T.B. would like to thank the BMBF - German Federal Ministry of Education and Research for supporting the project QuaLiZell in the Competence Cluster AQua (03XP0355B).

The color palette used in this report was generously provided by Anton Tsitsulin (see https://tsitsul.in/blog/coloropt/). This palette has been carefully optimized to ensure accessibility for color-blind readers and to maintain distinguishability when presented in black-and-white formats.

In order to improve the readability and language quality of this manuscript, ChatGPT 4o by OpenAI and Writer by DeepL were utilized during the writing process. It is important to note that the content and ideas presented in the manuscript were not generated by these language models, and the authors take full responsibility for the content. Their use was focused solely on improving fluency and correcting spelling errors. A final review and correction of the manuscript was performed by the authors to ensure accuracy and consistency.

Data and code availability

All analyzed data sets in this study are available for download at Zenodo under the doi: 10.5281/zenodo.11633769.

The code used for the generalized distribution of relaxation times method is part of the ec-idea software toolbox developed at the Chair of Electrical Energy Systems at the University of Bayreuth and is available online at https://www.ees.uni-bayreuth.de/en/ec-idea/index.html

Appendix A. Context of a Negative Resistance in the Generalized Cole-Cole Model

The generalized form of the Cole-Cole model can be used to define the impedance function of a resistive-inductive element by inserting a negative phasor φ in its equation:

$$Z_{\mathrm{RK}}(R,\,\varphi,\,\tau,\,j\omega) = Z_{R\phi}(R,\,-\varphi,\,\tau,\,j\omega) = \frac{R\cdot(j\omega\tau)^{\varphi}}{1+(j\omega\tau)^{\varphi}} \qquad [\mathrm{A}{\cdot}1]$$

The same can be achieved by using a negative resistance instead. However, this requires an additional correction term, which can be calculated by comparing both approaches:

$$
\begin{aligned}
Z_{R\phi}(-R,\,\varphi,\,\tau,\,j\omega) + \Theta &\overset{!}{=} Z_{R\phi}(R,\,-\varphi,\,\tau,\,j\omega)\\
\frac{-R}{1+(j\omega\tau)^{\varphi}} + \Theta &= \frac{R\cdot(j\omega\tau)^{\varphi}}{1+(j\omega\tau)^{\varphi}}\\
\Theta &= \frac{R\cdot(j\omega\tau)^{\varphi}}{1+(j\omega\tau)^{\varphi}} + \frac{R}{1+(j\omega\tau)^{\varphi}}\\
\Theta &= R\cdot\left(\frac{1}{1+(j\omega\tau)^{\varphi}} + \frac{(j\omega\tau)^{\varphi}}{1+(j\omega\tau)^{\varphi}}\right)\\
\Theta &= R\cdot\frac{1+(j\omega\tau)^{\varphi}}{1+(j\omega\tau)^{\varphi}}\\
\Leftrightarrow \Theta &= R
\end{aligned}
$$

It can be observed that the impedance function of a resistive-inductive element can be represented by the impedance function of a resistive-capacitive element when the polarization is considered negative and its value is added as an additional ohmic resistance.

Appendix B. Derivation of the Fredholm Integral Equation for the Generalized Cole-Cole Model

The underlying Fredholm integral of the DRT, defined as

$$Z(j\omega) = R_0 + \int_{-\infty}^{\infty}\frac{\gamma(\tau)}{1+j\omega\tau}\mathrm{d}\ln\tau, \qquad \text{[B·1]}$$

can be adapted to represent resistive-inductive and resistive-capacitive impedance features. For this, the integral is first extended to inherit the two distribution functions that are restricted to positive polarization. Next, the expression is rearranged and the two distribution functions are combined according to

$$\Upsilon = \gamma_{\mathrm{RC}} - \gamma_{\mathrm{RL}} \qquad \text{[B·2]}$$

to represent them with a single unconstrained distribution function:

$$
\begin{aligned}
Z(j\omega) &= R_{0,\mathrm{true}} + \int_{-\infty}^{\infty}\frac{\gamma_{\mathrm{RC}}}{1+j\omega\tau}\,\mathrm{d}\ln\tau\\
&\quad + \int_{-\infty}^{\infty}\frac{\gamma_{\mathrm{RL}}}{1+(j\omega\tau)^{-1}}\,\mathrm{d}\ln\tau\\
&= R_{0,\mathrm{true}} + \int_{-\infty}^{\infty}\frac{\gamma_{\mathrm{RC}}+\gamma_{\mathrm{RL}}\cdot j\omega\tau}{1+j\omega\tau}\,\mathrm{d}\ln\tau\\
&= R_{0,\mathrm{true}} + \int_{-\infty}^{\infty}\frac{\gamma_{\mathrm{RC}}-\gamma_{\mathrm{RL}}}{1+j\omega\tau} + \frac{\gamma_{\mathrm{RL}}\cdot(1+j\omega\tau)}{1+j\omega\tau}\,\mathrm{d}\ln\tau\\
&= R_{0,\mathrm{true}} + \int_{-\infty}^{\infty}\frac{\Upsilon}{1+j\omega\tau} + \gamma_{\mathrm{RL}}\,\mathrm{d}\ln\tau\\
&= R_{0,\mathrm{true}} + \int_{-\infty}^{\infty}\frac{\Upsilon}{1+j\omega\tau}\,\mathrm{d}\ln\tau + \int_{-\infty}^{\infty}\gamma_{\mathrm{RL}}\,\mathrm{d}\ln\tau
\end{aligned}
\qquad \text{[B·3]}
$$

It can be seen, that the substitution is adding an additional ohmic offset with its resistance equal to the total polarization of the resistive-inductive distribution function.

Appendix C. Derivation of the Analytical Distribution Function for the Generalized Cole-Cole Model

To get the analytical DRT function of a known element, we need the transfer function. E.g. for the Cole-Cole model, its given by Eq. 4:

$$Z_{R\phi}(j\omega) = \frac{R}{1+(j\omega\tau)^{\varphi}}$$

Inserted in Eq. 9:

$$\gamma(\tau)_{R\phi} = \frac{j}{2\pi}\cdot\left(Z\left(\frac{1}{\tau}\cdot e^{j\pi}\right) - Z\left(\frac{1}{\tau}\cdot e^{-j\pi}\right)\right)$$

this leads to

$$\gamma(\tau)_{R\phi} = \frac{j}{2\pi}\cdot\left(\frac{R}{1+\left(\frac{1}{\tau}\cdot e^{j\pi}\tau_{R\phi}\right)^{\varphi}} - \frac{R}{1+\left(\frac{1}{\tau}\cdot e^{-j\pi}\tau_{R\phi}\right)^{\varphi}}\right). \qquad \text{[C·1]}$$

Note that $(e^{\pm j\pi})^{\varphi} = e^{\pm j\pi\varphi}$ is a fractional multi-valued function. The complex function $Z(s)$ must be evaluated with s approaching the branch cut of the exponential term on the negative real axis from the upper and lower half-plane, respectively. Therefore, the limits $Z(-1/\tau + j0_+) \neq Z(-1/\tau + j0_-)$ act as a complex conjugate in the s-plane and the argument of Eq. 9 does not vanish. To simplify it further, we rearrange the inner terms separately. Additionally, for a better readability, we replace $\left(\frac{\tau_{R\phi}}{\tau}\right)^{\varphi}$ with T.

$$
\begin{aligned}
&\frac{R}{1+\left(\frac{1}{\tau}\cdot e^{\pm j\pi}\tau_{R\phi}\right)^{\varphi}}\\
&= R\frac{1}{1+T\cdot e^{\pm j\pi\varphi}}\\
&= R\frac{1+T\cdot e^{\mp j\pi\varphi}}{1+T^2+Te^{\mp j\pi\varphi}+Te^{\pm j\pi\varphi}}\\
&= R\frac{1+T\cdot e^{\mp j\pi\varphi}}{1+T^2+2T\cos(\pi\varphi)}\\
&= R\frac{T^{-1}+e^{\mp j\pi\varphi}}{T^{-1}+T+2\cos(\pi\varphi)}\\
&\text{Using } x+x^{-1} = 2\cosh(\ln x) \text{ results in}\\
&= \frac{R}{2}\frac{T^{-1}+e^{\mp j\pi\varphi}}{\cosh(\ln(T))+\cos(\pi\varphi)}
\end{aligned}
$$

Inserting this expression for both terms leads to:

$$
\begin{aligned}
\gamma(\tau)_{R\phi} &= \frac{j}{2\pi}\cdot\left(\frac{R}{2}\frac{T^{-1}+e^{-j\pi\varphi}}{\cosh(\ln(T))+\cos(\pi\varphi)}\right.\\
&\quad\left. - \frac{R}{2}\frac{T^{-1}+e^{j\pi\varphi}}{\cosh(\ln(T))+\cos(\pi\varphi)}\right)\\
\gamma(\tau)_{R\phi} &= \frac{j}{2\pi}\cdot\left(\frac{R}{2}\frac{-2j\sin(\pi\varphi)}{\cosh(\ln(T))+\cos(\pi\varphi)}\right)
\end{aligned}
$$

As can be seen, the DRT function for the Cole-Cole model is:

$$\gamma(\tau)_{R\phi} = \frac{R}{2\pi}\cdot\frac{\sin(\pi\varphi)}{\cosh(\varphi\cdot[\ln(\tau_{R\phi})-\ln(\tau)])+\cos(\pi\varphi)}. \qquad \text{[C·2]}$$

Appendix D. Derivative of the Real Part

The real part of the impedance is defined by

$$Z_{\mathrm{re}}(j\omega) = R_0 + \int_{-\infty}^{\infty}\Upsilon(\tau)\frac{1}{1+\omega^2\tau^2}\mathrm{d}\ln\tau \qquad \text{[D·1]}$$

For a discrete set of (measured) frequencies $\boldsymbol{\omega}$ and pre-set time constants $\boldsymbol{\tau}$ this can be simplified to

$$\mathbf{Z}_{\mathrm{re}} = R_0\mathbf{1} + \mathbf{A}_{\mathrm{re}}\boldsymbol{\Upsilon}. \qquad \text{[D·2]}$$

with **1** being a vector of ones, $\mathbf{A}_{re}$ the matrix containing the kernel function $\frac{1}{1+\omega^2\tau^2}$ evaluated at the frequency and time constant set points, and Υ the vector of polarizations at the pre-set time constants constituting the discrete distribution function. However the equation can be derived from $\ln(\omega)$

$$\frac{dZ_{re}(\omega)}{d\ln(\omega)} = \frac{dR_0}{d\ln(\omega)} + \frac{d}{d\ln(\omega)}\int_{-\infty}^{\infty}\frac{\Upsilon(\tau)}{1+\omega^2\tau^2}d\ln\tau$$

$$Z'_{re}(\omega) = \int_{-\infty}^{\infty}\Upsilon(\tau)\frac{d}{d\ln(\omega)}\left(\frac{1}{1+\omega^2\tau^2}\right)d\ln\tau$$

$$Z'_{re}(\omega) = \int_{-\infty}^{\infty}\Upsilon(\tau)\left(\frac{-2\omega^2\tau^2}{(1+\omega^2\tau^2)^2}\right)d\ln\tau$$

This can be simplified to

$$\mathbf{Z}'_{re} = \mathbf{A}'_{re}\Upsilon \qquad [D\cdot3]$$

Therefore, the real displacement R_0 becomes unnecessary when the DRT is calculated using the gradients.

ORCID

Christian Plank https://orcid.org/0000-0002-8345-1549
Michael A. Danzer https://orcid.org/0000-0002-4135-7263

References

1. K. S. Cole and R. H. Cole, "Dispersion and absorption in dielectrics I. Alternating current characteristics." *The Journal of Chemical Physics*, **9**, 341 (1941).
2. A. C. Lazanas and M. I. Prodromidis, "Electrochemical impedance spectroscopy-a tutorial." *ACS Measurement Science Au*, **3**, 162 (2023).
3. E. Barsoukov and J. Ross Macdonald, *Impedance Spectroscopy* (John Wiley & Sons, Nashville, TN) 3rd ed. (2018).
4. E. P. Randviir and C. E. Banks, "A review of electrochemical impedance spectroscopy for bioanalytical sensors." *Anal. Methods*, **14**, 4602 (2022).
5. X. Ma, A. Fischerauer, S. Haacke, and G. Fischerauer, "Determination of the bentonite content in molding sands using AI-enhanced electrical impedance spectroscopy." *Sensors*, **24** (2024).
6. V. Meiler, J. Pfeiffer, L. Bifano, C. Kandlbinder-Paret, and G. Fischerauer, "Approaches to detect microplastics in water using electrical impedance measurements and support vector machines." *IEEE Sens. J.*, **23**, 4863 (2023).
7. S. Dierickx, A. Weber, and E. Ivers-Tiffée, "How the distribution of relaxation times enhances complex equivalent circuit models for fuel cells." *Electrochim. Acta*, **355**, 136764 (2020).
8. T. E. Springer, T. A. Zawodzinski, M. S. Wilson, and S. Gottesfeld, "Characterization of polymer electrolyte fuel 413 cells using ac impedance spectroscopy." *J. Electrochem. Soc.*, **143**, 587 (1996).
9. M. J. Jørgensen, S. Primdahl, and M. Mogensen, "Characterization of composite SOFC cathodes using electrochemical impedance spectroscopy." *Electrochim. Acta*, **44**, 4195 (1999).
10. R. Li, J. Wu, H. Wang, and G. Li, "Prediction of state of charge of lithium-ion rechargeable battery with electrochemical impedance spectroscopy theory." *Proc. 2010 5th IEEE Conf. Ind. Electron. Appl. ICIEA*, **5th**, 684 (2010).
11. R. Ruffo, R. Fathi, D. J. Kim, Y. H. Jung, C. M. Mari, and D. K. Kim, "Impedance analysis of $Na_{0.44}MnO_2$ positive electrode for reversible sodium batteries in organic electrolyte." *Electrochim. Acta*, **108**, 575 (2013).
12. I. V. Krasnikova, M. A. Pogosova, A. O. Sanin, and K. J. Stevenson, "Toward standardization of electrochemical impedance spectroscopy studies of Li-ion conductive ceramics." *Chemistry of Materials*, **32**, 2232 (2020).
13. P. Vadhva, J. Hu, M. J. Johnson, R. Stocker, M. Braglia, D. J. L. Brett, and A. J. E. Rettie, "Electrochemical impedance spectroscopy for all-solid-state batteries: Theory, methods and future outlook." *Chem Electro Chem*, **8**, 1930 (2021).
14. M. Hahn, S. Schindler, L.-C. Triebs, and M. A. Danzer, "Optimized process parameters for a reproducible distribution of relaxation times analysis of electrochemical systems." *Batteries*, **5**, 43 (2019).
15. Q. Guo, V. R. Subramanian, J. W. Weidner, and R. E. White, "Estimation of diffusion coefficient of lithium in carbon using ac impedance technique." *J. Electrochem. Soc.*, **149**, A307 (2002).
16. F. Katzer, T. Rüther, C. Plank, F. Roth, and M. A. Danzer, "Analyses of polarisation effects and operando detection of lithium deposition in experimental half- and commercial full-cells." *Electrochimica Acta*, **436**, 141401 (2022).
17. F. Luo, H. H. Huang, L. P. Ni, and T. Li, "Rapid prediction of the state of health of retired power batteries based on electrochemical impedance spectroscopy." *J. Energy Storage*, **41**, 102866 (2021).
18. T. Rüther, W. Hileman, G. L. Plett, M. S. Trimboli, and M. A. Danzer, "Demystifying the distribution of relaxation times: A simulation-based investigation into the limits and possibilities of interpretation for lithium-ion batteries." *J. Electrochem. Soc.*, **171**, 060508 (2024).
19. M. Hahn, D. Rosenbach, A. Krimalowski, T. Nazarenus, R. Moos, M. Thelakkat, and M. A. Danzer, "Investigating solid polymer and ceramic electrolytes for lithium-ion batteries by means of an extended distribution of relaxation times analysis." *Electrochimica Acta*, **344**, 136060 (2020).
20. J. D. Huang, C. Meisel, N. P. Sullivan, A. Zakutayev, and R. O'Hayre, "Rapid mapping of electrochemical processes in energy-conversion devices." *Joule*, **8**, 2049 (2024).
21. L. Hennerici, P. Ficht, M. Schamel, U. Mansfeld, M. Linz, D. Paulus, J. Kita, M. A. Danzer, and R. Moos, "Lithium all-solid-state batteries fabricated at room temperature by the powder aerosol deposition method with garnet-type electrolyte and graded composite cathode." *Advanced Materials Technologies*, **10**, 2400745 (2024).
22. M. Ranz, B. Grabner, B. Schweighofer, H. Wegleiter, and A. Trattner, "Dynamics of anion exchange membrane electrolysis: Unravelling loss mechanisms with electrochemical impedance spectroscopy, reference electrodes and distribution of relaxation times." *Journal of Power Sources*, **605**, 234455 (2024).
23. J. Pati and R. S. Dhaka, "Mixed polyanionic $NaFe_{1.6}V_{0.4}(PO_4)(SO_4)2$@CNT cathode for sodium-ion batteries: electrochemical diffusion kinetics and distribution of relaxation time analysis at different temperatures." *Journal of Power Sources*, **609**, 234646 (2024).
24. J. Liu, K. Pan, H. Cho, M. Canova, and J.-H. Kim, "Deciphering the degradation mechanisms of nano-Si and micro-SiO anodes in lithium-ion battery full-cells using distribution relaxation times analysis." *Electrochimica Acta*, **500**, 144746 (2024).
25. T. Rüther, M. Schamel, C. Plank, F. Schomburg, F. Röder, and M. A. Danzer, "Cell-to-cell variation beyond parameter analysis—identification and correlation of processes in lithium-ion batteries using a combined distribution of relaxation times analysis." *Journal of Power Sources*, **587**, 233677 (2023).
26. S. Puls et al., "Benchmarking the reproducibility of all-solid-state battery cell performance." *Nat. Energy*, **9**, 1310–1320 (2024).
27. D. Semerukhin, A. Kubarkov, V. Sergeyev, O. Semenikhin, and E. Antipov, "Analysis of the distribution of relaxation times (DRT) responses of Li-ion cells as a function of their preparation conditions." *Electrochimica Acta*, **486**, 144092 (2024).
28. M. A. Danzer, "Generalized distribution of relaxation times analysis for the characterization of impedance spectra." *Batteries*, **5**, 53 (2019).
29. P. Korth Pereira Ferraz, R. Schmidt, D. Kober, and J. Kowal, "A high frequency model for predicting the behavior of lithium-ion batteries connected to fast switching power electronics." *Journal of Energy Storage*, **18**, 40 (2018).
30. I. Pivac and F. Barbir, "Inductive phenomena at low frequencies in impedance spectra of proton exchange membrane fuel cells—A review." *Journal of Power Sources*, **326**, 112 (2016).
31. A. Schiefer, M. Heinzmann, and A. Weber, "Inductive low-frequency processes in pemfc-impedance spectra." *Fuel Cells*, **20**, 499 (2020).
32. S. K. Roy, M. E. Orazem, and B. Tribollet, "Interpretation of low-frequency inductive loops in PEM fuel cells." *J. Electrochem. Soc.*, **154**, B1378 (2007).
33. N. Wagner and M. Schulze, "Change of electrochemical impedance spectra during co poisoning of the pt and Pt–Ru anodes in a membrane fuel cell (PEFC)." *Electrochimica Acta*, **48**, 3899 (2003), electrocatalysis:From Theory to Industrial Applications.
34. H. Sumi, H. Shimada, K. Watanabe, Y. Yamaguchi, K. Nomura, Y. Mizutani, and Y. Okuyama, "External current dependence of polarization resistances for reversible solid oxide and protonic ceramic cells with current leakage." *ACS Appl. Energy Mater.*, **6**, 1853 (2023).
35. J. Huang, M. Papac, and R. O'Hayre, "Towards robust autonomous impedance spectroscopy analysis: A calibrated hierarchical bayesian approach for electrochemical impedance spectroscopy (eis) inversion." *Electrochimica Acta*, **367**, 137493 (2021).
36. M. A. Danzer, C. Plank, and T. Rüther, "Electrochemical system analysis from impedance data to system identification." *Cell Reports Physical Science*, **5**, 102091 (2024).
37. J. Jacquelin, "The phasance concept: A review." *Current Topics in Electrochemistry*, **4**, 127 (1997).
38. A. Lasia, "The origin of the constant phase element." *The Journal of Physical Chemistry Letters*, **13**, 580 (2022).
39. S. Holm, T. Holm, and O. Martinsen, "Simple circuit equivalents for the constant phase element." *PLoS ONE*, **16**, e0248786 (2021).
40. E. Locorotondc, L. Pugi, L. Berzi, M. Pierini, S. Scavuzzc, A. Ferraris, A. G. Airale, and M. Carello, "Modeling and simulation of constant phase element for battery electrochemical impedance spectroscopy." *IEEE 5th International forum on Research and Technology for Society and Industry (RTSI)*, **2019**, 225 (2019).
41. C. Plank, T. Rüther, L. Jahn, M. Schamel, J. P. Schmidt, F. Ciucci, and M. A. Danzer, "A review on the distribution of relaxation times analysis: A powerful tool for process identification of electrochemical systems." *Journal of Power Sources*, **594**, 233845 (2024).
42. L. Wildfeuer, P. Gieler, and A. Karger, "Combining the distribution of relaxation times from eis and time-domain data for parameterizing equivalent circuit models of lithium-ion batteries." *Batteries*, **7**, 1 (2021).
43. E. Goldammer and J. Kowal, "Determination of the distribution of relaxation times by means of pulse evaluation for offline and online diagnosis of lithium-ion batteries." *Batteries*, **7** (2021).
44. R. He, Y. He, W. Xie, B. Guo, and S. Yang, "Comparative analysis for commercial li-ion batteries degradation using the distribution of relaxation time method based on electrochemical impedance spectroscopy." *Energy*, **263**, 125972 (2023).
45. E. Boj, S. Azizighalehsari, P. Venugopal, G. Rietveld, and T. Soeiro, "A distribution of relaxation time approach on equivalent circuit model parameterization to analyse

li-ion battery degradation." *11th International Conference on Power Electronics and ECCE Asia*, **11**, 1403 (2023).
46. B. A. Boukamp, "Fourier transform distribution function of relaxation times; application and limitations." *Electrochimica Acta*, **154**, 35 (2015).
47. A. Leonide, V. Sonn, A. Weber, and E. Ivers-Tiffée, "Evaluation and modeling of the cell resistance in anode-supported solid oxide fuel cells." *J. Electrochem. Soc.*, **155**, B36 (2008).
48. T. Hörlin, "Deconvolution and maximum entropy in impedance spectroscopy of noninductive systems." *Solid State Ionics*, **107**, 241 (1998).
49. T. Paul, P. W. Chi, P. M. Wu, and M. K. Wu, "Computation of distribution of relaxation times by tikhonov regularization for li ion batteries: usage of l-curve method." *Sci. Rep.*, **11**, 12624 (2021).
50. T. G. Bergmann and N. Schlüter, "Introducing alternative algorithms for the determination of the distribution of relaxation times." *Chemphyschem: A European Journal of Chemical Physics and Physical Chemistry*, **23**, e202200012 (2022).
51. R. M. Fuoss and J. G. Kirkwood, "Electrical properties of solids. viii. dipole moments in polyvinyl chloride-diphenyl systems." *J. Am. Chem. Soc.*, **63**, 385 (1941).
52. M. F. Rosenberg, *oder Die Regularisierung eines exponentiell schlecht gestellten Problems* (2001).
53. X. Zhao, S. Wang, S. Yuan, L. Cheng, and Y. Cai, "Multichannel sparse spike deconvolution based on dynamic time warping." *Acta Geophysica*, **69**, 783 (2021).
54. N. Schlüter, S. Ernst, and U. Schröder, "Finding the optimal regularization parameter in distribution of relaxation times analysis." *ChemElectroChem*, **6**, 6027 (2019).
55. M. Saccoccio, T. Wan, C. Chen, and F. Ciucci, "Optimal regularization in distribution of relaxation times applied to electrochemical impedance spectroscopy: Ridge and lasso regression methods - a theoretical and experimental study." *Electrochimica Acta*, **147**, 470 (2014).
56. C. Plank, T. Rüther, and M. A. Danzer, "Detection of non-linearity and non-stationarity in impedance spectra using an extended Kramers-Kronig test without overfitting." *International Workshop on Impedance Spectroscopy (IWIS)*, **2022**, 1 (2022).
57. I. Pivac, I. J. Halvorsen, D. Bezmalinovic, F. Barbir, and F. Zenith, (2020)"Low-frequency EIS intercept as a diagnostic tool for PEM fuel cells degradation." *Zenodo*, .